Uncertainty modeling of refraction effects in non-central camera calibration

Yu Lan, Mario Kolling, Alexander Dorndorf, Jens-André Paffenholz
Germany

Key words: LiDAR-camera MSS, camera calibration, ChArUco board, refraction model, uncertainty

SUMMARY

With the rapid adoption of LiDAR-camera multi-sensor systems (MSS) in industrial and intelligent perception, accurate calibration of camera intrinsics is critical for reliable sensor data fusion and environmental perception. Target-based camera calibration with ChArUco board or checkerboard is, however, limited to the quality of corner measurements. In practice these measurements carry uncertainties that propagates through the calibration pipeline and can bias camera intrinsics, distortion and calibration board pose with respect to the camera. Besides, in this work, to enable the camera to operate in harsh environments, the camera is enclosed in a protective housing with a front-mounted dome port. The dome port introduces refraction that perturbs ray geometry and invalidates the standard pinhole projection from 3D points to the image plane.
To address these challenges, this study incorporates a physical refraction model for an in-air dome-port camera into the imaging model. The uncertainties are explicitly modeled by assigning a covariance matrix to each detected ChArUco corner. These uncertainties are propagated to the estimated camera intrinsics, distortion, calibration board poses, and the decentering between the dome port center and the camera optical center. The resulting camera and dome port parameter estimations are accompanied by statistically justified covariance matrices, enabling uncertainty-aware residual weighting during optimization. The proposed modeling framework is expected to support future MSS integration tasks.

Uncertainty modeling of refraction effects in non-central camera calibration

Yu Lan, Mario Kolling, Alexander Dorndorf, Jens-André Paffenholz
Germany

1 INTRODUCTION

Camera intrinsic calibration is a prerequisite for obtaining metrically reliable information from images, because it establishes a consistent relationship between 2D image measurements and 3D coordinates when combined with an appropriate scene model. It is therefore essential not only for LiDAR-camera based multi-sensor systems (MSS), but also for any application that relies on accurate image-based measurements. To enable the system to operate in harsh environments, e.g., heavy rain or high humidity, cameras are mounted behind protective housings with a dome port. If the dome port center and camera optical center are not well mechanically adjusted, it will introduce air-glass-air refraction. This departs from the assumptions of a central pinhole model and introduces spatially varying distortions. If this refraction effect is ignored, standard calibration can lead to biased estimates of camera intrinsics and distortion parameters as well as the board pose, which in turn degrades geometric consistency.

Most dome-port-related literature targets underwater imaging. In parallel, mainstream calibration pipelines usually assume homoscedastic, isotropic corner noise or ignore measurement uncertainties altogether. In real scenes, however, sub-pixel corner measurement variance and anisotropy depend strongly on signal-to-noise ratio (SNR), blur, viewing angle, and partial occlusion. When these effects are not properly modeled, they can lead to suboptimal estimates and underestimated parameter covariances. Therefore, this research proposes a dome-port-aware camera calibration framework that: 1) models dome port refraction in air-glass-air medium and 2) propagates per-corner pixel-level covariance through the pinhole model and refraction model into a weighted estimation and uncertainty analysis. This produces the estimates of intrinsics, distortion and board pose that are less biased and equipped with well-calibrated confidence interval (CI). The resulting camera calibration may provide useful statistical priors for future LiDAR-camera in the context of MSS extrinsic calibration. In the present work, the investigation focuses on the camera subsystem and its refraction-aware calibration. This paper is organized as follows: Section 2 reviews the literatures of camera calibration, refraction modeling and uncertainty analysis. Section 3 presents the materials and sensor setup in this research, including the camera system and the specially designed calibration board. It describes the configuration of the imaging setup and the characteristics of the calibration target. Section 4 presents the camera calibration method and uncertainty factors in the camera measurements of ChArUco corners and the estimation of the covariance. The refraction model of the camera and dome port and the propagation of uncertainties from pixel

(px) level to camera intrinsics, distortion and calibration board poses. Section 5 presents the experimental results, focusing on the propagation of per-corner covariance to camera intrinsics and distortion, the estimation of the decentering (the dome port center coordinate on the camera frame) and calibration board poses. Section 6 discusses the results and directions for the future work.

2 STATE OF THE ART

In the camera calibration, Zhang (2000) introduced a flexible calibration method using only a planar target observed from multiple viewpoints, providing a closed-form linear initialization followed by maximum likelihood estimation (MLE)-based non-linear refinement. In addition, for pose estimation in camera calibration, the Perspective-n-Point (PnP) algorithm aims to estimate the camera pose from correspondences between 3D world points and their 2D image projections (Lepetit et al., 2009). In dome-port camera refraction modeling, Yang et al. (2021) developed a non-central refraction calibration using a universal spherical refraction model with coplanarity constraints and a modified perspective center for air-glass-air. They demonstrated that spherical covers induced distortions that are not adequately described by a standard central perspective model and they achieved robust, accurate calibration without explicit 3D object coordinates. She et al. (2022) showed that misalignment between the camera lens and a spherical dome port turns the system into an axial camera, proposed a non-iterative method to compute the center of refraction without precise media parameters, derived a 6th-degree forward-projection model for thin domes, and introduced a pure underwater calibration to estimate decentering for mechanical adjustment or photogrammetric correction. Elnashef and Filin (2022) integrated non-linear refraction rays covering thin and thick interfaces and the in-air (air-medium-air) configuration directly into the collinearity equations, showed that an off-center system is axial but can be made equivalent to central projection via slight parameter adjustment, and proposed a single-step centering procedure with sub-tenth-millimeter accuracy. In camera corner measurement, external factors such as lighting, blur, viewing angle, and partial occlusion degrade corner quality, ignoring this propagates error into the camera intrinsics, distortion and calibration board poses calculation. Building on the Harris-Stephens local auto-correlation framework (Harris & Stephens, 1988), Peng et al. (2019) used sub-pixel corner localization to estimate a covariance matrix for each checkerboard intersection. Skibicki et al. (2020) analyzed how the camera and its optics contribute to object-space position uncertainty and presented a methodology to estimate the combined standard uncertainty together with contribution of individual factors, assuming no external disturbances. Hagemann et al. (2022) focused on camera calibration uncertainty, introducing a resampling-based estimator that extends classical covariance to non-ideal conditions and a model-independent uncertainty metric, with bias detection used only to separate systematic error, the approach is validated on simulated and real cameras. Wang et al. (2022) pointed out that MLE based calibration implicitly assumes equal per-corner uncertainty. While pose and board slant effects could be mitigated by adequate sampling, sensor inhomogeneity induces heteroscedastic errors that cause overfitting. They estimated a per-corner uncertainty and used it as a weight in geometric

calibration down-weighting noisy corners and emphasizing precise ones and validated on an eight-camera dataset against OpenCV and recent methods.
Building on the observations above, this paper introduces per-corner covariance on the calibration target and propagate it through both the camera calibration as well as the camera and the dome-port refraction models. This uncertainty-aware formulation jointly estimates camera intrinsics and distortion, calibration board poses, and decentering, reweights observations by reliability, and thereby delivers more accurate results.

3 MATERIAL AND SETUP OF CAMERA CALIBRATION

The subject of this paper is a camera embedded in a LiDAR-camera based MSS for plant phenotyping tasks, (Fig. 1(a), right). To better utilize the MSS for observing the object, e.g., plant phenotypes, the camera to object distances range from 0.5 m to 1.5 m. Consequently, the calibration distance is adopted to the typical camera to object distance.
A hybrid calibration board having a ChArUco pattern is used (Fig. 1(a), left). The latter is primarily used for camera calibration and is surrounded by 4-fold and 8-fold targets originally designed for LiDAR-target feature extraction and LiDAR-camera extrinsic calibration. In the present work, only camera-based ChArUco measurement is used for calibration.

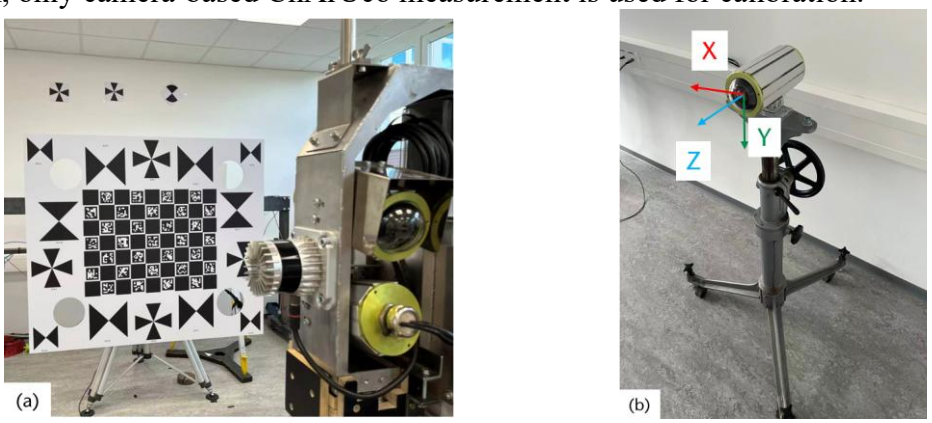

Fig. 1 (a) LiDAR-camera MSS and hybrid calibration board (b) Camera with dome port mounted on a stable tripod

The camera used in the MSS is the Allied Vision Alvium 1800U (Allied Vision, n.d.) shown in the Fig. 1(b) in its protective housing. For calibration purposes, it is mounted on a stable tripod to prevent movements while mounting or detaching the dome port. The lens mounted is the Kowa LM6FC24M | 1.1" 6.5 mm 24 MP, which is a wide-angle lens (Kowa, n.d.). The camera lens aperture is set to f/5.6, with the focus distance at ∼1 m. The technical parameters of the camera are shown in Table 1. Based on the technical information provided by the manufacturer, the dome port has a glass thickness of 5 mm, an inner radius $r_{in} = 32$ mm and an outer radius $r_{out} = 37$ mm. Throughout the experiments, the dome port was repeatedly mounted and detached. To ensure positional consistency across the mounting sequences, reference marks on the protective housing and dome port were applied so that the dome port could be mounted at the same axial depth each time to ensure a constant distance between the dome port center and

the camera optical center. The camera is not perfectly mechanical mounted inside the protective housing, which means that the optical center of the camera is not within the dome port center, this will result in refraction.

For camera calibration, the image acquisition was deliberately designed to ensure sufficient geometric diversity and robust parameter observability. The calibration board was observed from multiple positions and orientations to achieve full coverage of the image plane. In particular, images were captured with controlled viewing variations, including tilt and in-plane rotations of approximately 5° and 10° and with camera-to-object distances ranging from approximately 0.5 m to 1.5 m. In total, 58 images from multiple camera viewpoints were used for camera calibration. To further strengthen the network geometry, the calibration board was positioned such that, across the full image set, the ChArUco pattern jointly covered the entire sensor area. This strategy reduces parameter correlation and improves the stability of the intrinsic and refraction-related parameter estimation (Luhmann et al., 2023).

Table 1. Camera and lens parameters taken from the manufacturer specifications (Allied Vision, n.d., Kowa, n.d.)

Sensor	Sony IMX304, 1.1″
Sensor size	14.2 mm × 10.4 mm (diagonal: 17.6 mm)
Resolution	4112 px × 3008 px
Pixel pitch	3.45 µm
Focal length	6.5 mm (covers 1.1″)
Horizontal FOV	≈ 95.5°
Vertical FOV	≈ 77.3°
Diagonal FOV	≈ 107.7°

The ChArUco pattern is mainly used for camera intrinsics calibration and refraction modeling (Fig. 2(a)). Therefore, the dimensional accuracy of the ChArUco pattern is critical to the experiments. The dimensions of the ChArUco have been verified using a total station (Fig. 2(b)). The mean value of the length of each raster is 100.1 mm, whereby the error is [99.4 mm–100.7 mm], which is within the acceptable tolerance in this camera calibration processing.

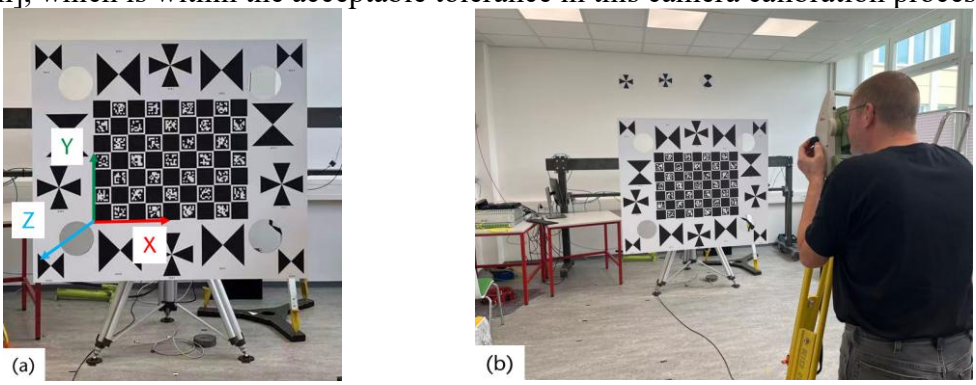

Fig. 2 (a) ChArUco pattern and the ChArUco coordinate system (b) Use of a total station to measure the corner points and verify the accuracy of the calibration target dimensions

The parameter of the ChArUco pattern is shown in Table 2. The ChArUco corners detection is performed using the OpenCV (4.13.0) library, i.e., the functions: *cv2.aruco.detectMarkers* and *cv2.aruco.interpolateCornersCharuco*. The ArUco marker detection in the ChArUco pattern is based on the function: *cv2.aruco.DetectorParameters_create.* The ArUco detection parameters are kept to be the same (Bradski & Kaehler, 2000; Garrido-Jurado et al., 2014).

Table 2. Dimension of the ChArUco target

Raster size	0.1 m
ArUco maker size	0.08 m
Dictionary	DICT 7×7 250
Number of rasters	32
Number of ArUco marker	31
Number of corners need to be measured by camera	48

4 METHOD

The experiment comprises two stages. Stage 1 without dome port mounting: for each view as inputs the ChArUco corners are measured and the covariance of $\boldsymbol{\Sigma}_{px,ij}$ are estimated, where $i = 1, \dots, M, M \in \mathbb{N}^+$, i indexes images and $j = 1, \dots, n_i,\ n_i \in \mathbb{N}^+$, j indexes corners within image i. A standard pinhole calibration is performed to estimate the following outputs: camera intrinsics $\boldsymbol{K}$ and lens distortion $\boldsymbol{d}$, together with their uncertainties $\boldsymbol{\Sigma}_{\boldsymbol{\theta\theta},cam}$. Furthermore, the calibration board poses ($\boldsymbol{R}_i$, $\boldsymbol{t}_i$) as well as the uncertainty $\boldsymbol{\Sigma}_{\boldsymbol{\theta\theta},pose,i}$ can also be estimated ($\boldsymbol{\theta}$ is the vector including camera intrinsics, lens distortion and calibration board pose).
Stage 2 with dome port mounting, refraction modeling: enhancing the inputs of stage 1 with the camera intrinsics and distortion and using the per-corner measurement covariance $\boldsymbol{\Sigma}_{px-d,ij}$, will lead to the weighting in the non-linear least-squares estimation of the refraction model. Using this uncertainty-aware refraction model, we estimate as outputs: the decentering vector $\mathbf{f}_{dec}$ (uncertainty $\boldsymbol{\Sigma}_{\boldsymbol{YY},dec}$) from the camera optical center to the dome port center, the calibration board pose ($\boldsymbol{R}_{dome,i}, \boldsymbol{t}_{dome,i}$) and the associated uncertainties of these estimates $\boldsymbol{\Sigma}_{\boldsymbol{YY},pose}$ ($\boldsymbol{Y}$ is the vector includes decentering and calibration board pose).
For each observation group, the camera acquires a pair of datasets at an identical ChArUco pose, one with and one without the dome port installed, so that the pose is matched across the two conditions.

4.1 Uncertainty factors

In the camera calibration, there are numerous factors that will influence the uncertainty of the camera calibration board corner measurement (Fig. 3). According to Wang et al. (2021), in terms of the image quality, the factors mainly include SNR, image blur, corner opening angle, or in-plane rotation across views.

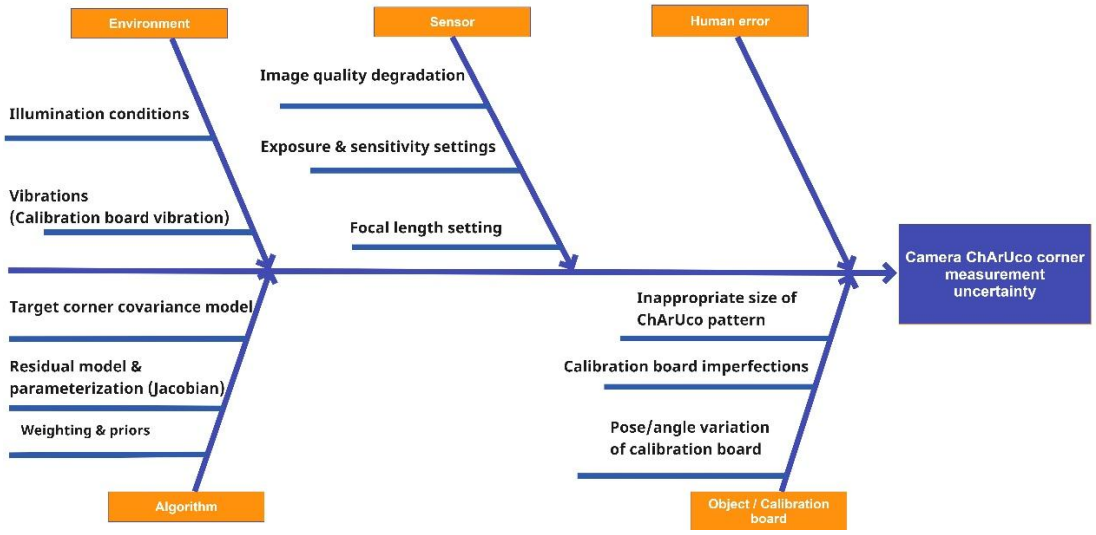

Fig. 3 Ishikawa (1990) diagram showing the uncertainty factors of the corner measurement in the camera calibration

Environment: To control the illumination, the experiment was done in an indoor lab environment with uniform and controllable lighting. All experiments were conducted under identical lighting conditions. The calibration board is mounted on a stable tripod to avoid vibrations.

Sensor: Exposure and sensitivity settings directly affect the SNR of the captured image, lower SNR leads to noisier corner measurement (Förstner & Gülch, 1987). Image blur and inconsistent imaging capability reduce the local gradient which degrades the accuracy of feature point localization. The focal length of the camera lens was fixed. The uncertainties associated with focal length and corner measurements will be addressed in future work.

Human error: Operator-induced procedural errors, whose impact on experimental uncertainty can be reduced through training, are beyond the scope of the present study and are not discussed further.

Reference system: From a reference-frame perspective, deterministic inter-frame coordinate transforms do not introduce additional noise. Uncertainty originates in the model and its parameters and is merely propagated to other frames via chained Jacobians. If these transforms are uncertain or unstable-particularly the calibration poses and the refraction parameters, these will become the dominant contributors to the overall camera calibration uncertainty.

Algorithm: From the algorithmic viewpoint, camera calibration uncertainty is driven by 3 modeling decisions: 1) how the per-corner pixel covariance $\boldsymbol{\Sigma}_{px,ij}$ (or $\boldsymbol{\Sigma}_{px-d,ij}$) is constructed, here we used 58 images total 2784 corners, which determines the resulting data weighting matrix $\boldsymbol{\Sigma}^{-1}$ used in the estimation process; 2) the projection (image-formation) model with its parametrization, which together determine the Jacobian $\boldsymbol{J}$ of the residuals; 3) and how prior information is integrated into the estimation process, such as estimated $\boldsymbol{K}$ or $\boldsymbol{d}$, which are required for estimating the calibration parameters of the dome port. Under a Laplace's

approximation around the maximum a posteriori (MAP) estimate, switching any of these modeling decisions will directly modify $\boldsymbol{\Sigma}^{-1}$ or $\boldsymbol{J}$ and thus the final uncertainty. In the stage of camera calibration and refraction modeling, this work does not propagate camera parameter posteriors between stages, just the per-corner pixel covariance is taken into account. Implementation details are given in Sections 4.1 to Section 4.3.

Object/Calibration board: To reduce interference, the calibration board material is usually chosen to have high rigidity, low reflectivity, and a flat surface. The most common choice is aluminium composite panel with a matte surface print. To address potential manufacturing tolerances of the ChArUco pattern, this work independently verified the ChArUco board dimensional accuracy using a total station (see Section 3).

In this paper, the measurement uncertainty of corner in the pixel plane is jointly determined by SNR, imaging blur, and viewing geometry. Wang et al. (2022) used the local auto-correlation matrix around each target corner and, by introducing a self-defined SNR γ with two normalizing operations, turn the multi-mapping into a single-valued relation that is stable across SNR, rotation angle, open angle of the detected control points, and blur. Based on this relation, the per-corner 2×2 inverse covariances is estimated in the pixel domain and used as weight in the weighted reprojection objective. The multi-mapping problem by incorporating a self-defined SNR γ and two normalizing operations. The SNR γ is defined as:

$$\gamma = \frac{(\text{white}-\text{black})^2}{\sigma^2} \quad (1)$$

where white and black are the mean digital number (DN) of pixels from the white blocks (the white margin surrounding the ArUco marker) and black blocks around the detected target corner. σ^2 is the image noise variance in the intensity domain.

Let (α, β) and (v_α, v_β) be the eigenvalues and eigenvectors of the local auto-correlation matrix $\boldsymbol{C}_{ac}$. $x = \frac{\alpha\beta}{\gamma^2\sigma^4}$ denotes the normalized point response and $y = 100\sqrt{\gamma}\,SD$ denotes the normalized standard deviation (SD). According to Wang et al. (2022), the function to predict the normalized SD from a normalized point response is built as:

$$f(x) = \frac{a}{x} + bx + c \quad (2)$$

Based on Eq. (1) and Eq. (2), the weighting matrix $\boldsymbol{\Sigma}_{px,ij}^{-1}$ of each target corner is (in the dome-port mounted camera, the weighting matrix is $\boldsymbol{\Sigma}_{px-d,ij}^{-1}$) estimated by:

$$\boldsymbol{\Sigma}_{px,ij}^{-1} = \left[v_\alpha, v_\beta\right] \cdot \begin{bmatrix} \frac{\alpha+\beta}{\beta}\left(\frac{100\sqrt{\gamma}}{f\left(\frac{\alpha\beta}{\gamma^2\sigma^4}\right)}\right)^2 & 0 \\ 0 & \frac{\alpha+\beta}{\alpha}\left(\frac{100\sqrt{\gamma}}{f\left(\frac{\alpha\beta}{\gamma^2\sigma^4}\right)}\right)^2 \end{bmatrix} \cdot \left[v_\alpha, v_\beta\right]^T \quad (3)$$

where the coefficients $(\alpha+\beta)/\beta$ and $(\alpha+\beta)/\alpha$ can ensure the estimated inverse covariance matrix had a similar uncertainty to the predicted SD. Based on Eq. (1) to Eq. (3), the covariance matrix is estimated for the ChArUco corner measurement in each image frame.

4.2 Pinhole model-based camera calibration

The camera calibration is performed in two steps. First, Zhang's method is used to obtain an initial estimate of $\boldsymbol{K}$ and $\boldsymbol{d}$. Second, a weighted maximum-likelihood refinement is performed that incorporates per-corner covariance. In Eq. (4), $s \in \mathbb{R}^+$ is an arbitrary scale factor. According to Zhang (2000), let $\boldsymbol{u}_{ij} = [u_{ij}, v_{ij}]^T$ denote an image pixel point and $\boldsymbol{X}_{ij} = [X_{ij}, Y_{ij}, Z_{ij}]^T$ a point in 3D space. The homogeneous coordinates are used: $\widetilde{\boldsymbol{u}}_{ij} = [u_{ij}, v_{ij}, 1]^T$ and $\widetilde{\boldsymbol{X}}_{ij} = [X_{ij}, Y_{ij}, Z_{ij}, 1]^T$. The extrinsic transformation $[\boldsymbol{R}_i \mid \boldsymbol{t}_i]$ is used to transform the ChArUco frame into the camera frame. $\boldsymbol{R}_i \in SO(3)$ is the rotation matrix, while $\boldsymbol{t}_i \in \mathbb{R}^3$ is the translation vector. Under the standard pinhole camera model, their relationship is:

$$s\widetilde{\boldsymbol{u}}_{ij} = \boldsymbol{K}[\boldsymbol{R}_i \mid \boldsymbol{t}_i]\widetilde{\boldsymbol{X}}_{ij} \qquad (4)$$

$$\text{with } \boldsymbol{K} = \begin{bmatrix} f_x & s_{sk} & c_x \\ 0 & f_y & c_y \\ 0 & 0 & 1 \end{bmatrix} \qquad (5)$$

In the matrix $\boldsymbol{K}$, c_x *and* c_y denote the coordinates of the principal point, f_x and f_y denote the scale factors in image axes. s_{sk} is the parameter which describes the image axes skewness, which is defined as follows $s_{sk} = 0$ (Zhang, 2000).

Let $\boldsymbol{X}_{ij} = [X_{ij}, Y_{ij}]^T$ denote a point on the calibration target ($Z = 0$). Its homogeneous coordinate is $\widetilde{\boldsymbol{X}}_{ij} = [X_{ij}, Y_{ij}, 1]^T$. For such points, the pinhole model reduces to a planar projective mapping between the model plane and the image:

$$s\widetilde{\boldsymbol{u}}_{ij} = \boldsymbol{H}_{homo}\,\widetilde{\boldsymbol{X}}_{ij} \qquad (6)$$

$$\text{with } \boldsymbol{H}_{homo} = \boldsymbol{K}\,[\boldsymbol{r}_1\ \boldsymbol{r}_2\ \boldsymbol{t}_i] \qquad (7)$$

where $\boldsymbol{r}_1, \boldsymbol{r}_2$ are the first two columns of the rotation matrix $\boldsymbol{R}_i$ (since $Z = 0$). The 3×3 homography $\boldsymbol{H}_{homo}$ is defined only up to a non-zero scalar multiple.

Given the wide-angle lens used in the present setup (Section 3), lens distortion is modeled using the Brown–Conrady distortion model with the OpenCV rational radial extension (Brown, 1971; OpenCV, n.d.). The distortion is parameterized by the 8 coefficients (6 radial and 2 tangential terms) $\boldsymbol{d} = [k_1\ k_2\ p_1\ p_2\ k_3\ k_4\ k_5\ k_6]$ (Cvišić et al., 2022). This choice is motivated by prior findings that rational models better capture large distortions typical of wide-angle optics (Tang et al., 2017). The practical necessity of individual distortion terms is not assumed a priori, instead, it is evaluated via covariance propagation (Section 5.1) and discussed with respect to model complexity and parameter observability (Section 6). For wide-angle optics, radial distortion is typically the dominant component, while tangential distortion may also be present depending on lens-sensor alignment. The adopted distortion model is given below. In Eq. (8) and Eq. (9) and Eq. (10), $(x'',\ y'')$ are the distorted normalized image coordinates and (u, v) are the pixel coordinates, r^{nc} is the radial distance in normalized coordinate.

$$\begin{bmatrix} u \\ v \end{bmatrix} = \begin{bmatrix} f_x x'' + c_x \\ f_y y'' + c_y \end{bmatrix} \qquad (8)$$

where

$$\begin{bmatrix} x'' \\ y'' \end{bmatrix} = \begin{bmatrix} x' \frac{1+k_1(r^{nc})^2+k_2(r^{nc})^4+k_3(r^{nc})^6}{1+k_4(r^{nc})^2+k_5(r^{nc})^4+k_6(r^{nc})^6} + 2p_1x'y' + p_2((r^{nc})^2 + 2x'^2) + s_1(r^{nc})^2 + s_2(r^{nc})^4 \\ y' \frac{1+k_1(r^{nc})^2+k_2(r^{nc})^4+k_3(r^{nc})^6}{1+k_4(r^{nc})^2+k_5(r^{nc})^4+k_6(r^{nc})^6} + 2p_2x'y' + p_1((r^{nc})^2 + 2y'^2) + s_3(r^{nc})^2 + s_4(r^{nc})^4 \end{bmatrix} \quad (9)$$

with

$$(r^{nc})^2 = x'^2 + y'^2 \quad (10)$$

and

$$\begin{bmatrix} x' \\ y' \end{bmatrix} = \begin{bmatrix} X^c/Z^c \\ Y^c/Z^c \end{bmatrix} \quad (11)$$

In Eq. (9), (x', y') are the undistorted normalized image coordinates. k_1 to k_6 are the radial coefficients, p_1 and p_2 are the tangential distortion coefficients, s_1 to s_4 are the thin prism distortion coefficients, this work fixes them to zero and does not estimate them further. In Eq. (11), (X^c, Y^c, Z^c) are the 3D coordinates in the camera coordinate frame, where c is for camera coordinate system.

Based on the camera calibration, the covariance from the ChArUco corner measurement should be introduced to the refinement of the camera calibration. However, Zhang (2000) refinement is a MLE non-linear optimization, with the implicit assumption that all image corner points share the same pixel noise. This study refined parameters from $\boldsymbol{K}$ and $\boldsymbol{d}$ via a weighted-MLE that incorporates per-corner covariance from ChArUco corner measurement. In Eq. (12), $\boldsymbol{u}_{ij} \in \mathbb{R}^2$ is the measured pixel coordinate $[u_{ij}, v_{ij}]^T$, $\hat{\boldsymbol{u}}_{ij}(\boldsymbol{\Theta}) \in \mathbb{R}^2$ is the predicted pixel coordinate from the forward projection according to Eq. (4). $\boldsymbol{\Theta}$ is the parameter vector to be estimated which includes: camera intrinsic parameters (f_x, f_y, c_x, c_y), $\boldsymbol{d}$ and per-view board poses $(\boldsymbol{R}_i, \boldsymbol{t}_i)$. $\boldsymbol{\varepsilon}_{px,ij} \in \mathbb{R}^2$ is the reprojection residual in pixels. In Eq. (13), $\boldsymbol{\Sigma}_{px,ij}^{-1}$ is the per-corner pixel weight calculated by Eq. (1) to Eq. (3). While Zhang's method provides an initialization, it implicitly assumes homoscedastic pixel noise (Zhang, 2000). To account for heteroscedastic and anisotropic corner uncertainty, we subsequently refine the parameters using a weighted MLE within a Gauss–Newton least-squares adjustment, where per-corner covariances define the observation uncertainty model. Thus, Zhang's method (as implemented in OpenCV) is used only for initialization, whereas the final estimates follow a weighted adjustment, enabling uncertainty propagation and statistically interpretable parameter covariances.

$$\boldsymbol{\varepsilon}_{px,ij} = \boldsymbol{u}_{ij} - \hat{\boldsymbol{u}}_{ij}(\boldsymbol{\Theta}) \quad (12)$$

$$\underset{\boldsymbol{\Theta}}{argmin} \sum_{i=1}^{M} \left(\sum_{j=1}^{n_i} \left(\boldsymbol{\varepsilon}_{px,ij}^T \boldsymbol{\Sigma}_{px,ij}^{-1} \boldsymbol{\varepsilon}_{px,ij} \right) \right) \quad (13)$$

In Eq. (13), $\sum_{i=1}^{M} \sum_{j=1}^{n_i}$ is the sum of all the residuals of all the image and corresponding corners. Where $\boldsymbol{\Sigma}_{px,ij}^{-1} \in \mathbb{R}^{2\times2}$ is the weighting matrix which can be summarized in the overall block-diagonal weight matrix in the following Eq. (14).

$$\boldsymbol{\Sigma}_{px}^{-1} = \begin{bmatrix} \boldsymbol{\Sigma}_{px,11}^{-1} & \cdots & \boldsymbol{0}_{2\times2} \\ \vdots & \ddots & \vdots \\ \boldsymbol{0}_{2\times2} & \cdots & \boldsymbol{\Sigma}_{px,Mn_M}^{-1} \end{bmatrix} \quad (14)$$

In this paper the per-view calibration board pose $(\boldsymbol{R}_i, \boldsymbol{t}_i)$ is formed in a minimal representation: each pose is parametrized by $\boldsymbol{\xi}_i = [\boldsymbol{\omega}_i^T, \boldsymbol{t}_i^T]^T \in \mathbb{R}^6$, where $\boldsymbol{\omega}_i \in \mathbb{R}^3$ is calculated by $\boldsymbol{R}_i$ (Faugeras, 1993). Accordingly, $\boldsymbol{\Theta} = [f_x, f_y, c_x, c_y, \boldsymbol{d}^T, \boldsymbol{\xi}_1^T, \ldots, \boldsymbol{\xi}_M^T]^T$, the partition camera

intrinsics and distortion are $[f_x,\ f_y, c_x, c_y, \boldsymbol{d}^T]^T$ and camera pose is $[\boldsymbol{\xi}_1^T, \ldots, \boldsymbol{\xi}_M^T]^T$, with stacked residuals $\boldsymbol{\varepsilon}_{px,ij}$ and Jacobian $\boldsymbol{J}_{\boldsymbol{\theta},px} = \partial \boldsymbol{\varepsilon}_{px} / \partial \boldsymbol{\theta}$ over all images and corresponding corners (Triggs et al., 1999). Under the Gauss–Newton approximation to the least-squares Hessian, the covariance of the parameter estimate $\hat{\boldsymbol{\theta}}$ is approximated by Eq. (15).

$$\boldsymbol{\Sigma}_{\boldsymbol{\theta}} \approx \boldsymbol{J}_{\boldsymbol{\theta},px}^T \boldsymbol{\Sigma}_{px} \boldsymbol{J}_{\boldsymbol{\theta},px} = \begin{bmatrix} \boldsymbol{\Sigma}_{\boldsymbol{\theta\theta},cam} & \boldsymbol{\Sigma}_{\boldsymbol{\theta},cam-pose} \\ \boldsymbol{\Sigma}_{\boldsymbol{\theta},pose-cam} & \boldsymbol{\Sigma}_{\boldsymbol{\theta\theta},pose} \end{bmatrix} \quad (15)$$

Where $\boldsymbol{\Sigma}_{\boldsymbol{\theta}}$ is the Gauss–Newton approximation to the least squares Hessian. The Hessian block $\boldsymbol{\Sigma}_{\boldsymbol{\theta\theta},cam}$ associated with the intrinsics and distortion and the $\boldsymbol{\Sigma}_{\boldsymbol{\theta\theta},pose}$ associated with ChArUco board pose (Triggs et al., 1999).

4.3 Dome-port refraction modeling and uncertainty propagation

Introducing a dome port in front of the camera induces refraction. In underwater photogrammetry a common practice, also emphasized by Kahmen & Luhmann (2022), is to mechanically align the lens entrance pupil to the dome port center. This configuration produces air-like ray paths, so the field of view and effective focal length are essentially preserved. Any small residuals due to imperfect alignment are typically absorbed by standard distortion calibration. Due to experimental constraints, it is challenging to mechanically align the dome port center with the lens entrance pupil. To address this challenge, a non-central refraction model (Fig. 4) is introduced following Yang et al. (2021) and She et al. (2022). Accordingly, we consider two configurations in the experiments: (i) imaging through the dome port and (ii) a reference configuration without the dome port.

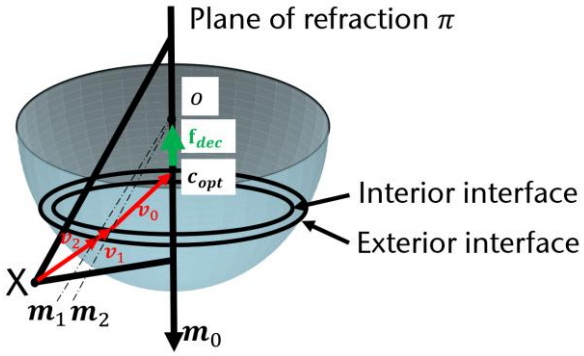

Fig. 4 Geometric model of the dome port according to Yang et al. (2021) and She et al. (2022)

According to Yang et al. (2021), in Fig. 4, the entire camera ray (including the ray inside the dome port $\boldsymbol{v}_0$, the refracted ray $\boldsymbol{v}_1$ and the incoming ray $\boldsymbol{v}_2$) and all the normals (the normal to the exterior and interior interface $\boldsymbol{m}_1$ and $\boldsymbol{m}_2$, respectively and the unified axis $\boldsymbol{m}_0$) lie in the same plane $\boldsymbol{\pi}$. Therefore, the geometric model is built in the plane of refraction (POR), $\boldsymbol{o}$ is the dome port center and $\boldsymbol{c}_{opt}$ is the camera optical center. The projected point $\hat{\boldsymbol{u}}_{ij}$ of the world point $\boldsymbol{X}_i$ depends on the known $\boldsymbol{K}$ and $\boldsymbol{d}$ (Section 4.2), the dome port parameters $(r_{in},\ r_{out},\ n)$

with n as the refraction index of the dome port. The decentering $\mathbf{f}_{dec}$ (in the camera coordinate system) as well as the calibration board poses with respect to camera ($\boldsymbol{R}_{dome,i}, \boldsymbol{t}_{dome,i}$) and also the $\mathbf{p}_{\text{refrac}}(\cdot)$, which is the refraction forward projection model for a dome-port camera (Yang et al., 2021). $\boldsymbol{u}_{ij}$ is the measured value of the pixel coordinate. The pixel residual for each observation using the refraction projection model is given in Eq. (16).

$$\boldsymbol{\varepsilon}_{dome,ij} = \boldsymbol{u}_{ij} - \hat{\boldsymbol{u}}_{ij} = \boldsymbol{u}_{ij} - \mathbf{p}_{\text{refrac}}\left(\boldsymbol{K}, \boldsymbol{d}, \mathbf{f}_{dec}, r_{in}, r_{out}, n, \boldsymbol{R}_{dome,i}, \boldsymbol{t}_{dome,i}, \boldsymbol{X}_{ij}\right) \in \mathbb{R}^2 \quad (16)$$

where $\boldsymbol{\varepsilon}_{dome,ij}$ is the residual of each corner. The unknown parameters in this POR model are $\mathbf{f}_{dec}, \boldsymbol{R}_{dome,i}, \boldsymbol{t}_{dome,i}$. Set $\boldsymbol{Y}$ to be the parameter vector that includes decentering $\mathbf{f}_{dec}$ and per-view calibration board poses ($\boldsymbol{R}_{dome,i}, \boldsymbol{t}_{dome,i}$). The per-corner pixel noise covariance $\boldsymbol{\Sigma}_{px-d,ij}$, calculated by Eq. (1) to Eq. (3). Within the Gauss–Newton least-squares framework, stacking all observation, the object by Gauss–Newton is in Eq. (17).

$$\underset{\boldsymbol{Y}}{argmin} \sum_{i=1}^{M}\left(\sum_{j=1}^{n_i}\left(\boldsymbol{\varepsilon}_{dome,ij}^{T}\boldsymbol{\Sigma}_{px-d,ij}^{-1}\boldsymbol{\varepsilon}_{dome,ij}\right)\right) \quad (17)$$

Then the weighting matrix $\boldsymbol{\Sigma}_{px-d,ij}^{-1}$is stacked in Eq. (18):

$$\boldsymbol{\Sigma}_{px-d}^{-1} = \begin{bmatrix} \boldsymbol{\Sigma}_{px-d,11}^{-1} & \cdots & \mathbf{0}_{2\times2} \\ \vdots & \ddots & \vdots \\ \mathbf{0}_{2\times2} & \cdots & \boldsymbol{\Sigma}_{px-d,Mn_M}^{-1} \end{bmatrix} \quad (18)$$

Each pose $\left(\boldsymbol{R}_{dome,i}, \boldsymbol{t}_{dome,i}\right)$ is parametrized by $\boldsymbol{\xi}_{dome,i} = [\boldsymbol{\omega}_{dome,i}^{T}, \boldsymbol{t}_{dome,i}^{T}]^{T} \in \mathbb{R}^6$, where $\boldsymbol{\omega}_{dome,i} \in \mathbb{R}^3$ is calculated by $\boldsymbol{R}_{dome,i}$. The parameter vector $\boldsymbol{Y} = [\mathbf{f}_{dec}, \boldsymbol{\xi}_{dome,1}^{T}, \ldots, \boldsymbol{\xi}_{dome,1}^{T}]^{T}$ to be estimated, includes the decentering as well as the calibration board pose. Taking the Jacobian: $\boldsymbol{J}_{\boldsymbol{Y},dome} = \frac{\partial \boldsymbol{\varepsilon}_{dome}}{\partial \boldsymbol{Y}}$, the covariance of the estimated parameters (include the estimated $\mathbf{f}_{dec}$and $\boldsymbol{R}_{dome,i}, \boldsymbol{t}_{dome,i}$) can be estimated according to Eq. (19) (Triggs et al., 1999).

$$\boldsymbol{\Sigma}_{\boldsymbol{Y}} \approx \boldsymbol{J}_{\boldsymbol{Y},dome}^{T}\boldsymbol{\Sigma}_{px-d}\boldsymbol{J}_{\boldsymbol{Y},dome} = \begin{bmatrix} \boldsymbol{\Sigma}_{\boldsymbol{YY},dec} & \boldsymbol{\Sigma}_{\boldsymbol{Y},dec-pose} \\ \boldsymbol{\Sigma}_{\boldsymbol{Y},pose-dec} & \boldsymbol{\Sigma}_{\boldsymbol{YY},pose} \end{bmatrix} \quad (19)$$

where the decentering parameter is corresponded to the Hessian block $\boldsymbol{\Sigma}_{\boldsymbol{YY},dec}$ and the calibration board pose is corresponded to the Hessian block $\boldsymbol{\Sigma}_{\boldsymbol{YY},pose}$.

5 EXPERIMENT RESULTS

5.1 Camera calibration without dome port

This work explicitly models the per-corner covariance $\boldsymbol{\Sigma}_{px,ij}$ and shows how pixel-level uncertainties propagate to the estimated camera intrinsics and distortion. Based on Eq. (12) to Eq. (13), a Q-Q plot of the squared Mahalanobis distances: $d_{ma,ij}^{2} = \varepsilon_{px,ij}^{T}\Sigma_{px,ij}^{-1}\varepsilon_{px,ij}$ against the theoretical χ_2^2 quantiles are used. Each dot denotes one ChArUco corner in each image frame. This figure is used to assess whether residuals are properly whitened and to flag anomalies under the current weighting model. Points close to 45° reference line (slope ≈ 1) means empirical quantiles of $d_{ma,ij}^{2}$ match χ_2^2 quantiles, which indicates residuals are properly whitened under the current weighting model (Garrett, 1989; Piché, 2016).

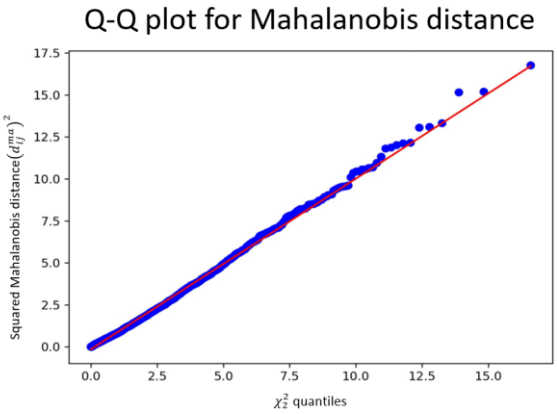

Fig. 5 Q-Q of Mahalanobis $d_{ma,ij}^2$ and χ_2^2

Points follow the 45° reference line across most quantiles, indicating that under the $\boldsymbol{\Sigma}_{px,ij}$, the residuals are properly whitened and no global rescaling of per-corner covariance is needed. A slight lift at the extreme upper tail suggests a few difficult corners or locally under-estimated uncertainty, consistent with mild heavy tail behavior.

To assess camera calibration accuracy is used the per-view image reprojection error (RPE), defined as the root-mean-square (RMS) pixel distance between the detected ChArUco corners and their projections given the estimated $\boldsymbol{K}$,$\boldsymbol{d}$ and per-view calibration board pose ($\boldsymbol{R}_i$,$\boldsymbol{t}_i$) (Fig. 6).

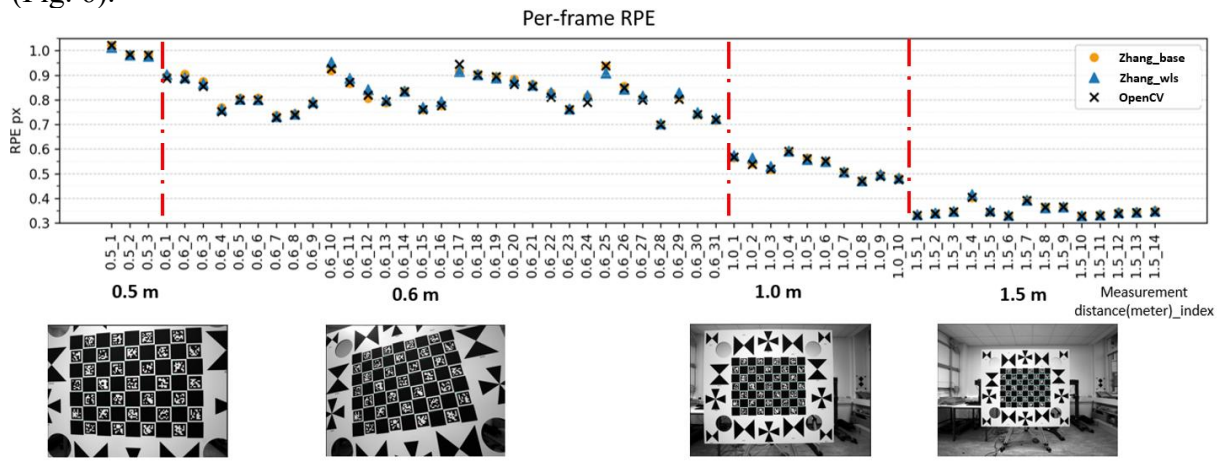

Fig. 6 RPE of the Zhang-base, Zhang-wls OpenCV method & the distance information

Per-frame RPE (px) for 3 solvers: Zhang-base (equal weight), Zhang-wls (per-corner covariance introduced), and OpenCV's `calibrateCameraCharuco` also equal weights (Bradski & Kaehler, 2000; Garrido-Jurado et al., 2014). During calibration, some frames with excessively high RPE were excluded. The three data series almost overlap across all frames: most RPE values lie between 0.3 and 1.0 px and show a gradual decrease with the measurement distance increase, indicating comparable calibration accuracy across methods and showing that incorporating pixel-level covariance into camera calibration yields no significant improvement in accuracy. This also aligns with Wang et al. (2022) view: a key determinant of whether

covariance can markedly improve reprojection accuracy is the consistent imaging capability. This will be analyzed in the future work. The small sawtooth-like fluctuations visible in Fig. 6 are likely related to frame-wise variations in the network geometry and corner spatial coverage, which can introduce small fluctuations in the RMS even under otherwise stable imaging conditions. The global RPE for Zhang-wls, Zhang-base, and OpenCV are all ≈ 0.70 px. Shorter distances 0.5 m and 0.6 m have larger RPE because, under a wide-angle lens, with the ChArUco board nearly fills the frame and many corners fall near the image periphery. At f/5.6 with focus set to ∼1 m, parts of the target fall outside the depth of field, degrading sub-pixel corner localization. In addition, many corners lie in the image periphery, where radial distortion and off-axis aberrations are stronger, making measurements more error-prone (Yan et al., 2020).

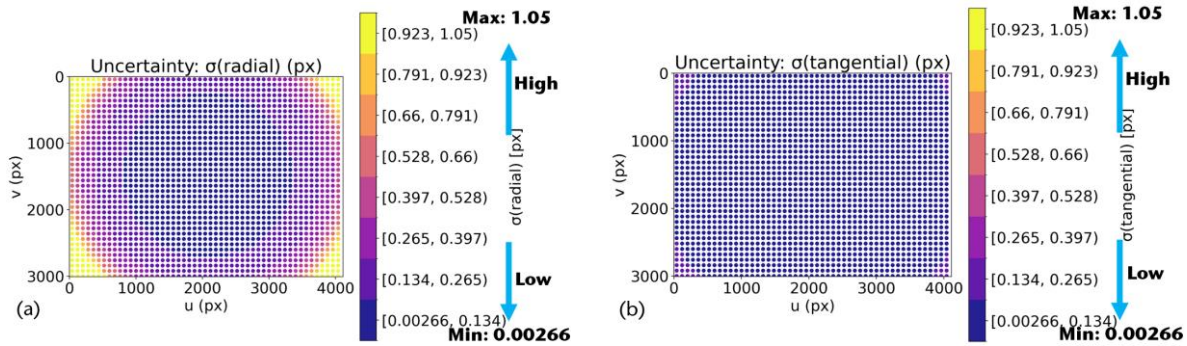

Fig. 7 Uncertainty maps of image distortion due to the covariance of the intrinsics and distortion (a) radial component, (b) tangential component. Values denote 1-σ in px.

After estimating the covariance of the camera intrinsics and distortion parameters, this work propagates it to the image plane using first-order uncertainty propagation. In Fig. 7(a), radial standard deviation σ_{rad} increases monotonically with field radius and peaks in the corners at 0.9 to 1.05 px, the central region is much lower (about 0.1 to 0.3 px). The map of radial distortion is ring-like and uncertainties in the intrinsics and radial-distortion are amplified at large radius. The relatively larger radial uncertainty at the image periphery is consistent with the wide-angle optics and the increase sensitivity between radial distortion parameters and off-axis rays, which amplifies the propagated uncertainty in the outer field of view. Fig. 7(b) shows that the tangential component is much smaller and highly uniform: most locations are ≤ 0.13 px with only a slight rise near the outer border, indicating that uncertainty from tangential distortion contributes little to the overall error budget. The near-uniform and low tangential uncertainty suggests limited observability of the tangential distortion parameters under the present imaging geometry. While a sensor noise floor may contribute to the observed lower bound, the overall pattern indicates that the tangential terms are weakly constrained in our setup. Consequently, introducing higher-order tangential terms would likely provide only marginal benefit. More generally, the covariance results support the adopted distortion parameterization by providing quantitative evidence on parameter observability and coupling, and by indicating which terms are well supported by the data and which are not.

5.2 Camera refraction modeling with dome port

In the camera refraction modeling, according to the POR model from Yang et al. (2021) and She et al. (2022), the decentering $\mathbf{f}_{dec}$ as well as the calibration board poses $(\boldsymbol{R}_{dome,i}, \boldsymbol{t}_{dome,i})$ are estimated. The estimated decentering represents a misalignment between the camera optical center and the dome port center, which deviates from the single effective viewpoint assumption of a central pinhole camera. Therefore, a non-central refraction model is required to capture the resulting systematic geometric effects introduced by the dome port particularly for off-axis rays. The estimation of the $\mathbf{f}_{dec}$,with and without introducing weight, are shown in Fig. 8.

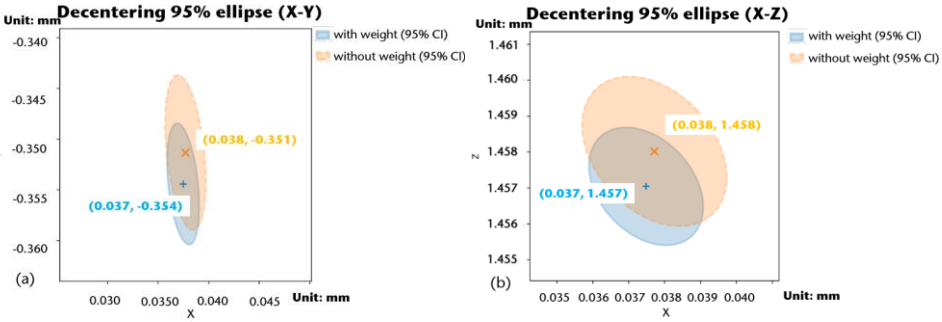

Fig. 8 Coordinate and uncertainty of the $\mathbf{f}_{dec}$ (a) X-Y direction (b) X-Z direction

In Fig. 8, the estimation of the coordinate (in the camera frame) (X, Y) of the decentering $\mathbf{f}_{dec}$ is (0.04 mm, −0.4 mm) for the weighted as well as for the unweighted estimation. In Z direction, the value is 1.5 mm for the weighted and unweighted estimate. The 95% CI uncertainty ellipse with weight estimation is smaller than without weight estimation, indicating lower overall uncertainty. By roughly physical measuring and computing the distance between the camera optical center and the dome port center. The roughly physical measurement in X and Y direction are close to 0.0 mm, and for the Z direction the physical measurement is about 1 mm to 5 mm, which shows the approximation is within an acceptable level.

Given a decentering estimation between the camera center and the dome port center, we estimate the ChArUco board pose for each image with the dome port attached $(\boldsymbol{R}_{dome,i}, \boldsymbol{t}_{dome,i})$. To isolate dome port effects while accounting for ChArUco corner measurement uncertainty, Fig. 9 compares the estimated poses obtained with covariance propagation against those obtained without corner-covariance propagation for the two scenarios without the dome port (Fig. 9(a)) use and with the dome port (Fig. 9(b)). In addition, during data acquisition, images are captured in pairs. One with dome port and one without while the ChArUco board remains rigidly fixed, so any pose discrepancy arises from the dome port or uncertainty propagation rather than changes in the position and orientation of the calibration target.

In the scenario without a dome port (Fig. 9(a)), introducing the weighting yields translation, i.e., pose, differences that remain close to 0, indicating that the geometric solution is essentially unchanged. This behavior is consistent with the RPE results in Section 5.1, where weighting mainly affects the estimated parameter uncertainties rather than the pose itself. With the dome

port installed (Fig. 9(b)), the impact of weighting becomes markedly larger and more structured, most notably in the axial, i.e., X, Y and Z components. The ΔZ difference is approximately constant within distance intervals and shows step-like changes at the interval boundaries, suggesting that a common-mode axial offset, primarily induced by dome port refraction, dominates the pose estimation. Overall, Fig. 9 indicates that in the with dome scenario, the refractive geometry dominates the pose solution, while covariance-based weighting plays a secondary role by redistributing residual influence and refining uncertainty rather than compensating the dome-induced systematic bias. In other words, for the dome-port-free scenario, covariance-based weighting primarily affects the estimated uncertainties rather than shifting the geometric optimum. Under the dome port scenario, the pose differences become stronger and more structured, and ΔZ shows a step-like behavior. This is consistent with dome-induced refractive ray bending. It may also indicate a deviation from a single effective viewpoint, for instance due to decentering. Together, these effects can amplify small geometric perturbations into noticeable orientation changes, particularly for off-axis observations. Alternatively, the structured differences may also reflect limitations or mismatches of the adopted refraction model, which can interact with the weighting and lead to distance-dependent pose discrepancies.

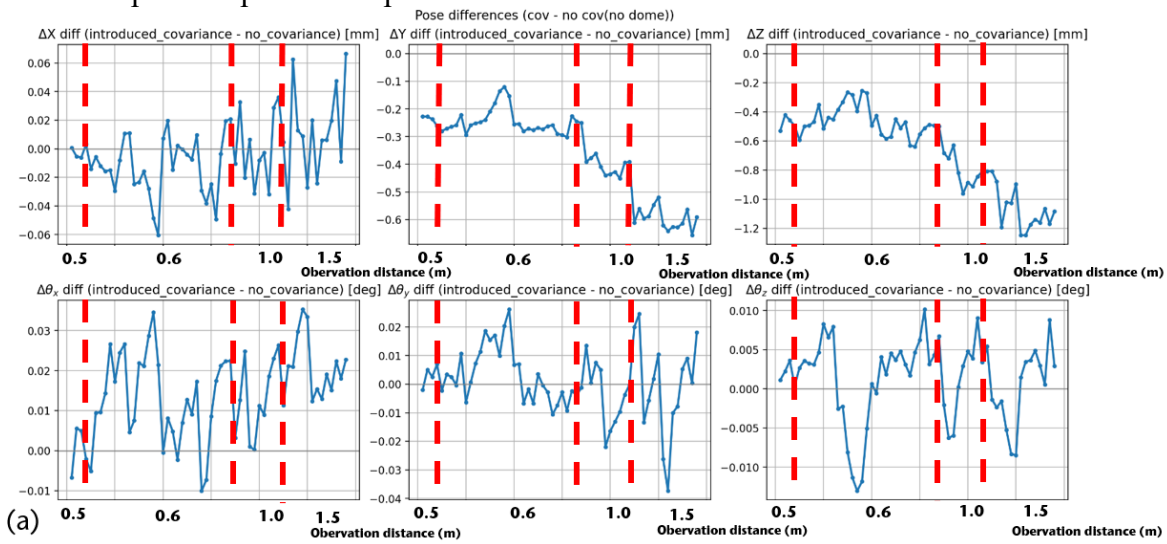

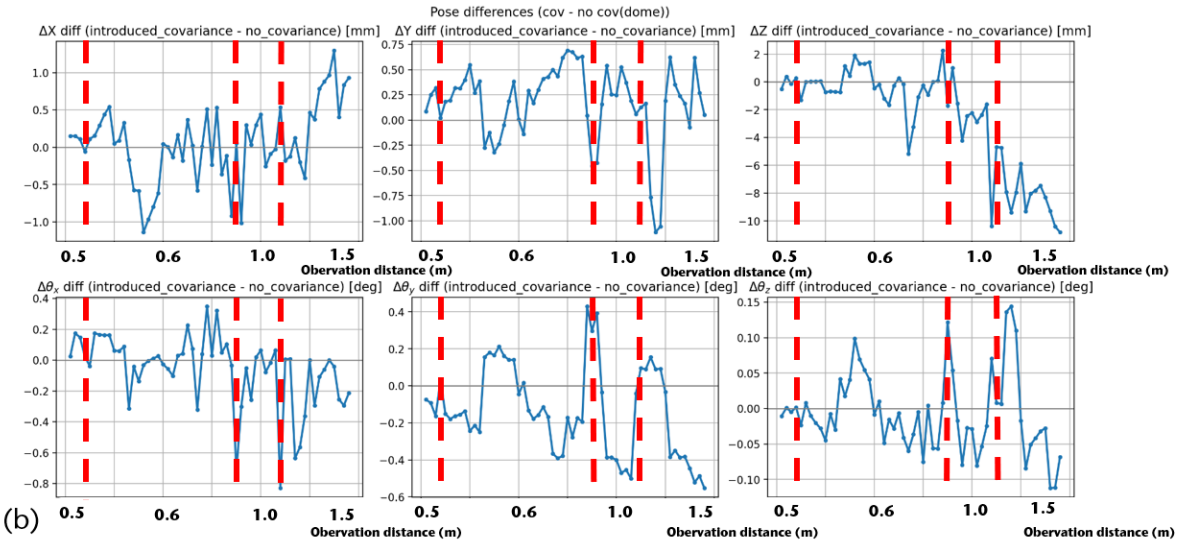

Fig. 9 Difference of the poses between camera and ChArUco observation distance (a) Pose difference from camera calibration with and without covariance introduce (no dome port) (b) Pose difference from camera refraction modeling with and without covariance introduce (with dome port). A representative image illustrating the observation distance is shown in Fig. 6.

6 CONCLUSION AND TO DO IN THE FUTURE

In this paper, from the Q-Q plot of the squared Mahalanobis distances and χ^2_2, indicating that the residuals are properly whitened. A small upper-tail excess suggests a few hard corners or mild heavy tailed noise. In the image, radial uncertainty increases from the center of the image to the corners, whereas the tangential component remains smaller and more uniform. Fig. 7(b) suggests that the tangential distortion parameters are weakly observable under the present configuration. While a sensor noise floor may contribute to the apparent lower bound, adding higher-order tangential terms is therefore expected to yield only marginal improvements. In the decentering estimation, with covariance, the 95% CI uncertainty ellipses become tighter, this indicates reduced uncertainty, additionally, the estimates $\mathbf{f}_{dec}$ is within the expected range. In Section 5, based on the Gauss–Newton covariance approximation, the parameter uncertainty is jointly determined by corner measurement noise, Jacobian-based parameter sensitivity, and the parameter coupling of the chosen model, including correlations introduced by the dome port decentering parameters. Fig. 9(a) shows only marginal differences between weighted and unweighted pose estimates in the dome-port-free scenario, indicating that under the present controlled imaging conditions the corner noise is relatively homogeneous and therefore has limited leverage on the geometric optimum. In contrast, Fig. 9(b) exhibits stronger and more structured pose differences under the dome port scenario, most notably a step-like behavior in ΔZ. This suggests that dome-induced refractive geometry, possibly coupled to the jointly estimated decentering parameters, dominates the estimation behavior, such that small changes in weighting can translate into noticeable pose differences. Overall, the evidence from Fig. 9

indicates that, for the present setup, the dominant error contribution is primarily refraction-driven rather than being dominated by pixel-level heteroscedastic corner noise.

From a practical perspective, the mechanical stability of the camera-dome assembly determines how many additional parameters are meaningfully observable. In highly stable and well-centered systems, decentering may be negligible and a standard central model may be sufficient. In contrast, in compact camera housings where mechanical tolerances are difficult to guarantee, additional decentering parameters can become relevant and help to absorb systematic refractive effects. In the present setup, the estimated decentering magnitude supports the use of a non-central model. Nevertheless, over-parameterization remains a potential risk in practical deployments and should be controlled by observability checks and model-selection criteria.

Future work will validate the weighting frame work based on ground-truth references. The Monte Carlo simulation will also be used in this work. Furthermore, the refraction model should be optimized. Immediate next steps should also focus on investigating how uncertainties in camera intrinsics and distortion (no dome port) propagate to camera refraction modeling with a dome port. Moreover, future work aims to develop a unified framework for uncertainty handling spanning imaging, geometry, and environmental factors. Specifically, we will explicitly account for focal-range coupling, small intrinsic drifts, and dome-port assembly tolerances. These uncertainties will be propagated consistently through the pipeline, from camera calibration to the estimation of the calibration-board pose in the camera frame. This unified treatment may also support future MSS integration tasks.

REFERENCES

Allied Vision, n.d. Alvium 1800 U-1236. Available at: https://www.alliedvision.com/en/products/area-scan-cameras/alvium/alvium-u/view/1134 (accessed 27 February 2026).

Bradski, G. and Kaehler, A., 2000. OpenCV. Dr. Dobb's journal of software tools, 3(2), pp.1-81.

Brown, D.C., 1971. Close-range camera calibration. Photogrammetric engineering, 37(8), pp.855-866.

Cvišić, I., Marković, I. and Petrović, I., 2022. Enhanced calibration of camera setups for high-performance visual odometry. Robotics and autonomous systems, 155, p.104189. https://doi.org/10.1016/j.robot.2022.104189

Elnashef, B. and Filin, S., 2022. Geometry, calibration, and robust centering procedures for refractive dome-port based imaging systems. ISPRS Journal of Photogrammetry and Remote Sensing, 194, pp.132-151. https://doi.org/10.1016/j.isprsjprs.2022.10.001

Förstner, W. and Gülch, E., 1987. A fast operator for detection and precise location of distinct points, corners and center of circular features. In Proc. ISPRS intercommission conference on fast processing of photogrammetric data (Vol. 6, pp. 281-305).

Faugeras, O., 1993. Three-dimensional computer vision: a geometric viewpoint. MIT press.

Garrido-Jurado, S., Muñoz-Salinas, R., Madrid-Cuevas, F.J. and Marín-Jiménez, M.J., 2014. Automatic generation and detection of highly reliable fiducial markers under occlusion. Pattern Recognition, 47(6), pp.2280-2292. https://doi.org/10.1016/j.patcog.2014.01.005

Garrett, R.G., 1989. The chi-square plot: a tool for multivariate outlier recognition. Journal of Geochemical Exploration, 32(1-3), pp.319-341. https://doi.org/10.1016/0375-6742(89)90071-X
Harris, C. and Stephens, M., 1988. A combined corner and edge detector. In Alvey vision conference (Vol. 15, No. 50, pp. 10-5244). https://doi.org/10.5244/C.2.23
Hagemann, A., Knorr, M., Janssen, H. and Stiller, C., 2022. Inferring bias and uncertainty in camera calibration. International Journal of Computer Vision, 130(1), pp.17-32. https://doi.org/10.1007/s11263-021-01528-x
Ishikawa, K. and Loftus, J.H., 1990. Introduction to quality control (Vol. 98). Tokyo: 3A Corporation.
Kowa, n.d. LM6FC24M | 1.1″ 6.5 mm 24 MP C-mount lens. Available at: https://www.kowa-lenses.com/de/LM6FC24M-1.1-6.5mm-24MP-C-mount-Objektiv/12185 (accessed 27 February 2026).
Kahmen, O. and Luhmann, T., 2022. Monocular photogrammetric system for 3D reconstruction of welds in turbid water. PFG–Journal of Photogrammetry, Remote Sensing and Geoinformation Science, 90(1), pp.19-35. https://doi.org/10.1007/s41064-022-00191-2
Luhmann, T., Robson, S., Kyle, S. and Boehm, J., 2023. Close-range photogrammetry and 3D imaging. Walter de Gruyter GmbH & Co KG. https://doi.org/10.1515/9783111029672
Lepetit, V., Moreno-Noguer, F. and Fua, P., 2009. EP n P: An accurate O (n) solution to the P n P problem. International journal of computer vision, 81(2), pp.155-166. https://doi.org/10.1007/s11263-008-0152-6
OpenCV, n.d. Camera Calibration and 3D Reconstruction. OpenCV Documentation. Available at: https://docs.opencv.org/4.x/d9/d0c/group__calib3d.html (accessed 08 August 2025).
Peng, S. and Sturm, P., 2019. Calibration wizard: A guidance system for camera calibration based on modelling geometric and corner uncertainty. In Proceedings of the IEEE/CVF International Conference on Computer Vision (pp. 1497-1505). https://doi.org/10.1109/ICCV.2019.00158
Piché, R., 2016. Online tests of Kalman filter consistency. International Journal of Adaptive Control and Signal Processing, 30(1), pp.115-124. https://doi.org/10.1002/acs.2571
She, M., Nakath, D., Song, Y. and Köser, K., 2022. Refractive geometry for underwater domes. ISPRS Journal of Photogrammetry and Remote Sensing, 183, pp.525-540. https://doi.org/10.1016/j.isprsjprs.2021.11.006
Skibicki, J., Golijanek-Jędrzejczyk, A. and Dzwonkowski, A., 2020. The influence of camera and optical system parameters on the uncertainty of object location measurement in vision systems. Sensors, 20(18), p.5433. https://doi.org/10.3390/s20185433
Tang, Z., Von Gioi, R.G., Monasse, P. and Morel, J.M., 2017. A precision analysis of camera distortion models. IEEE Transactions on Image Processing, 26(6), pp.2694-2704. https://doi.org/10.1109/TIP.2017.268600
Triggs, B., McLauchlan, P.F., Hartley, R.I. and Fitzgibbon, A.W., 1999, September. Bundle adjustment—a modern synthesis. In International workshop on vision algorithms (pp. 298-372). Berlin, Heidelberg: Springer Berlin Heidelberg. https://doi.org/10.1007/3-540-44480-7_21

Wang, K., Liu, C. and Shen, S., 2022. Geometric calibration for cameras with inconsistent imaging capabilities. Sensors, 22(7), p.2739. https://doi.org/10.3390/s22072739
Yang, W., Zhang, X., Ma, H., Zhang, G. and Yang, G., 2021. Non-central refractive camera calibration using co-planarity constraints for a photogrammetric system with an optical sphere cover. Optics and Lasers in Engineering, 139, p.106487. https://doi.org/10.1016/j.optlaseng.2020.106487
Yan, F., Liu, Z., Pan, X. and Shen, Y., 2020. High-accuracy calibration of cameras without depth of field and target size limitations. Optics Express, 28(19), pp.27443-27458. https://doi.org/10.1364/OE.402826
Zhang, Z., 2000. A flexible new technique for camera calibration. IEEE Transactions on pattern analysis and machine intelligence, 22(11), pp.1330-1334. https://doi.org/10.1109/34.888718

CONTACTS

Y. Lan, M.Sc.; M. Kolling, M.Sc.; A. Dorndorf, M.Sc.; Prof. Dr. J-A. Paffenholz
Clausthal University of Technology, Institute of Geotechnology and Mineral Resources, Geomatics for Underground Systems
Erzstr. 18, 36878 Clausthal-Zellerfeld, Germany Email: yu.lan@tu-clausthal.de